DEFAULT MODE NETWORK FUNCTIONAL CONNECTIVITY IN THE POSTICTAL STATE AFTER ELECTROCONVULSIVE THERAPY

TIJN STOLK

Abstract

The postictal state comprises of neurological and clinical symptoms such as unconsciousness or cognitive impairments. The most scientifically supported underlying pathophysiological mechanism is postictal vasoconstriction-mediated hypoperfusion. Besides, postictal symptomatology may be related to disrupted default mode network (DMN) functioning, as diminished functional DMN connectivity was present in patients with disorders of consciousness. This study investigates functional connectivity of the DMN after electroconvulsive therapy (ECT)-induced seizures in patients with major depressive disorder. One baseline resting-state functional magnetic resonance imaging (rs-fMRI) scan (before start of the ECT-course) and one postictal rs-fMRI scan (approximately one hour after ECT) were acquired from eighteen patients. We identified the DMN using Independent Component Analysis (ICA). Mean network connectivity strength was obtained by averaging the normalized parameter estimates from dual regression. Parcellation of the DMN resulted in 38 nodes, from which an undirected weighted graph was created based on the partial correlation of each node pair. We performed a graph theoretical analysis using clustering coefficient and characteristic path length to analyze efficiency of information segregation and integration, respectively. Paired samples t-tests were used to identify differences between baseline and postictal network measures. An analysis of covariance obtained associations between changes in DMN connectivity and both seizure duration and the time between the ECT-induced seizure and rs-fMRI acquisition. We observed a decrease in clustering coefficient ($p = 0.032$) whereas no changes were observed for neither connectivity strength nor characteristic path length ($p = 0.51$ and $p = 0.57$, respectively). A longer seizure duration was associated with a stronger decrease in clustering coefficient ($p = 0.041$) and a stronger increase in characteristic path length ($p = 0.019$) compared to baseline. The time between ECT and rs-fMRI acquisition was negatively associated with the difference in characteristic path length compared to baseline ($p = 0.014$). This study established disruptions in functional connectivity of the DMN in the postictal state. Longer seizures are associated with a stronger postictal decrease in both DMN segregation and integration.

Keywords: Postictal state, DMN, functional connectivity, segregation, integration

Supervisors
Julia C. M. Pottkämper
Freek ten Doesschate
David G. Norris

Affiliation
Radboud University, Nijmegen, The Netherlands
Donders Centre for Cognition, Nijmegen, The Netherlands

Significance

The default mode network (DMN) consists of several brain areas, including the precuneus, posterior cingulate cortex, bilateral inferior parietal cortices, and medial prefrontal cortex (Broyd et al., 2009). DMN activity is associated with internal mental processes and has been suggested to play an important role in the regulation of consciousness (Crone et al., 2011, 2015; Demertzi et al., 2014; Greicius et al., 2008; Norton et al., 2012; Vanhaudenhuyse et al., 2010). Impaired DMN activity may, therefore, underlie the symptomatology of the postictal state. Graph theory is a relatively novel method in brain imaging that can be used to reveal network connectivity abnormalities in neurological and psychiatric conditions (Rubinov & Sporns, 2010). By applying a small number of neurobiologically relevant and easily computable measures on predefined nodes in a brain network, important topological properties can be quantified (Rubinov & Sporns, 2010). The graph measures clustering coefficient and characteristic path length, for instance, describe how well adjacent nodes tend to cluster together and the capability of distant nodes to integrate in a network, respectively (Rubinov & Sporns, 2010; Watts & Strogatz, 1998). In the context of functional brain networks, the clustering coefficient reflects the ability for specialized processing to occur within localized brain areas, whilst the characteristic path length reflects the ability of a network to rapidly combine information from distributed brain areas (Rubinov & Sporns, 2010). The higher the clustering coefficient and the lower the characteristic path length, the more efficient information segregation and integration in a network. In this study, these graph measures are used in order to shed more light on the functional connectivity of the DMN in the postictal state on top of mean connectivity strength only.

Introduction

Epilepsy is one of the most common neurological disorders, as approximately 1% of the worldwide population suffers from epilepsy (Stafstrom & Carmant, 2015). Epilepsy reduces a patient's quality of life significantly, as a result of the seizures itself, as well as neurological, cognitive, or psychiatric symptoms occurring after epileptic seizures (de Boer, 2014; Fisher & Schachter, 2000; Pottkämper et al., 2020; Steiger & Jokeit, 2017). These symptoms are defined as the postictal state and consist of unconsciousness, unresponsiveness, confusion, delirium, headaches, nausea, amnesia, cognitive impairments, and in rare cases even psychoses (Pottkämper et al., 2020, 2021). The duration and severity of symptoms may vary between patients (Krauss & Edwards, 2014; Ohira et al., 2019; Pottkämper et al., 2020). Depending on the clinical manifestations, the postictal state may last from several seconds (altered states of consciousness) to minutes and hours (cognitive and physical symptoms) and days to weeks (psychiatric symptoms) (Pottkämper et al., 2020). Seizure duration seems to be associated with longer and more severe postictal symptoms (Farrell et al., 2017; Krauss & Edwards, 2014; Ohira et al., 2019).

The underlying pathophysiological mechanisms of the postictal state remain poorly understood. Up until now, several hypotheses such as neuronal exhaustion, neurotransmitter depletion, as well as altered concentrations of potassium, adenosine, nitric oxide and opiate receptors have been suggested to explain postictal symptoms (Fisher & Schachter, 2000; Pottkämper et al., 2020). However, most evidence currently points towards to the vasoconstriction-mediated hypoperfusion hypothesis, which suggests that postictal symptoms may arise as a result of vasoconstriction-mediated hypoperfusion and hypoxia in regions across the brain (Farrell et al., 2016, 2017; Pottkämper et al., 2020; Wolff, 2020). Support for this hypothesis was found in epilepsy patients, who had a decreased cerebral blood flow (CBF) in seizure onset zones during the first hour after seizures (Farrell et al., 2016).

Given the nature of the symptoms, diminished functioning of the default mode network (DMN) may underlie the symptomatology of the postictal state. The DMN consists of several brain areas including the precuneus, posterior cingulate cortex, bilateral inferior parietal cortices, and the medial prefrontal cortex (Broyd et al., 2009). DMN activity is associated with internal mental processes such as perspective-taking, emotion regulation, and remembering the past (Broyd et al., 2009; Manning & Steffens, 2016; Raichle et al., 2001). The DMN has been suggested to play an important role in regulation of consciousness, as DMN connectivity is diminished in patients with consciousness impairments such as vegetative state, coma and minimally conscious state (Crone et al., 2011, 2015; Demertzi et al., 2014; Greicius et al., 2008; Norton et al., 2012; Vanhaudenhuyse et al., 2010). Likewise, the DMN is functionally disrupted in dissociative amnesia and mild cognitive impairment patients (Garcés et al., 2014; Taïb et al., 2023). Additionally, several studies suggested that a dysfunctional DMN contributes to interictal cognitive impairments and ictal unconsciousness (Gotman et al., 2005; Laufs, 2012; Laufs et al., 2007; Lui et al., 2008). Thus, impaired DMN activity may be associated with the symptoms observed in the postictal state. Postictal functioning of the DMN, however, has not yet been studied.

The present study aimed to investigate functional connectivity of the DMN in the postictal state. Investigating the postictal state is challenging due to the spontaneous nature of seizures, making participation in clinical trials impractical. For this reason, electroconvulsive therapy (ECT) was used as this treatment elicits seizures in a well-controlled environment (McNally & Blumenfeld, 2004; Pottkämper et al., 2021). We used resting-state functional MRI (rs-fMRI) data acquired approximately one hour after ECT-induced seizures in order to examine postictal DMN connectivity compared to baseline. We hypothesize that mean network connectivity strength, as well as information segregation and integration in the DMN are diminished in the postictal state. In addition, we assessed if both seizure duration and the time between the ECT-induced seizure and rs-fMRI are associated with a postictal change in DMN connectivity. We expect that longer seizures, as well as a shorter period of time between seizure and rs-fMRI are associated with a stronger disruption in DMN connectivity.

Methods

Study Design

In this study, twenty patients were included who participated in a prospective clinical randomized trial with cross-over design in which the effects of vasoconstriction-mediating drugs nimodipine and acetaminophen were investigated to alleviate postictal symptoms. Patients with a treatment-resistant major depressive disorder undergoing ECT at Rijnstate Hospital in Arnhem, the Netherlands were included. Baseline rs-fMRI scans were performed within two weeks prior to start of ECT-course, whereas postictal rs-fMRI scans were performed approximately one hour post-ECT. As study intervention, patients either received acetaminophen, nimodipine, or a 50cc cup of water (i.e., placebo) up to two hours before an ECT-session.

Inclusion and exclusion criteria

Inclusion criteria were adulthood (> 17 years) with a current clinical diagnosis of a depressive episode (i.e. unipolar, bipolar, schizoaffective), an indication for ECT (i.e., medication resistant depressive disorder), and willingness and ability to give oral and written informed consent. Exclusion criteria were contraindications for MRI or chronic use of acetaminophen, calcium-antagonists or non-steroidal anti-inflammatory drugs which cannot be paused less than two days before an ECT-session.

ECT procedure

ECT is a widely used neuromodulating technique for treatment-resistant depression in which a generalized tonic-clonic seizure is elicited by administering short electrical stimuli to the cranium while patients are under general anesthesia (Kropotov, 2016; Murray et al., 2012). Patients received ECT according to standard treatment guidelines in the Netherlands and by using right unilateral (UL) or bifrontotemporal (BL) electrode placement (Broek, 2010; d'Elia, 1970).

The ECT stimuli were bidirectional, square wave and single brief pulses (1 ms) with a constant current (0.9 Ampère) and delivered by the Thymatron System IV device (Somatics Incorporation Lake Bluff, Illinois, USA). Patients were pre-oxygenated at 100% O2, anesthetized (etomidate 0.2-0.3 mg/kg) and ventilated until spontaneous respiration. Muscle relaxation was achieved by administering succinylcholine (0.5-1 mg/kg). In case of postictal hyperactive delirium, patients were given midazolam for sedation.

Data acquisition

MRI data were acquired on a 3T Philips Ingenia MR scanner with a 15 channel Philips dStream HeadSpine coil. The rs-fMRI data were obtained using 3D gradient-and-spin-echo (GRASE) readout module with the following parameters: repetition time (TR) = 2000 ms, echo time (TE) = 27 ms, flip angle (FA) = 90^0, field of view (FOV) = 230 × 230 mm, data matrix size = 128 × 128, slice thickness = 3 mm, slice gap = 0 mm, 160 volumes. The FOV was aligned to the anterior – posterior commissure line, after which the dorsal part of the FOV was rotated approximately 20^0 in the caudal direction. Prior to scanning, patients were asked to stay awake and move the least possible. Additionally, a T1-weighted scan was acquired before the rs-fMRI acquisition during the same scanning session, using the following parameters: TR = 7.5 ms, TE = 46 ms, FA = 8^0, FOV = 256 × 238 mm, data matrix size = 512 × 512, slice thickness = 1.77 mm, slice gap = 0 mm and 145 sagittal slices.

Data preprocessing

Preprocessing of the rs-fMRI data was performed using fMRIPrep 21.0.2 (Esteban et al., 2018), which is based on Nipype 1.6.1 (Gorgolewski et al., 2011). A B0-nonuniformity image was created based on multiple echo-planar imaging (EPI) references, which was used to correct the T1w image for intensity non-uniformity. The T1w image was subsequently skull-stripped and brain tissue segmented, after which it was used as a reference for volume-based spatial normalization to MNI152NLin6Asym space. For the rs-fMRI data, one BOLD reference was used to estimate head-motion parameters for spatiotemporal filtering, after which it was co-registered to the T1w reference. Framewise displacement (FD) was calculated as confounding time-series. Automatic removal of motion artifacts was performed using ICA-AROMA. BOLD time-series were normalized into standard space. Details and references of all fMRIPrep preprocessing steps are described in Appendix A. The remaining preprocessing steps of the rs-fMRI data included skull-stripping, spatial smoothing (FWHM = 6 mm), nuisance regression of cerebrospinal fluid and white matter, removal of the first five volumes for steady-state and, lastly, high-pass filtering (cutoff frequency = 0.007 Hz). Scans that retained at least 4 minutes of sufficiently motion-free data (i.e., mean FD < 0.6 mm and maximum FD < 2 mm) were included for analysis.

Default Mode Network extraction

In order to select a group-based DMN specific to patient population, a probabilistic Independent Component Analysis (ICA) as implemented in FSL's MELODIC has been carried out on the concatenated rs-fMRI data of all baseline and postictal scans (Beckmann et al., 2005; Beckmann & Smith, 2004; Hyvärinen, 1999). The DMN was extracted as the fourth from a total of 25 components (Figure 1A). A z-score threshold of 4 was applied to the DMN component in order to create a spatial mask of the DMN component (Figure 1B), consisting of the voxels that correlated strongest within the DMN. This mask served as input for the network connectivity strength analysis, as well as DMN parcellation.

Figure 1
Default mode network

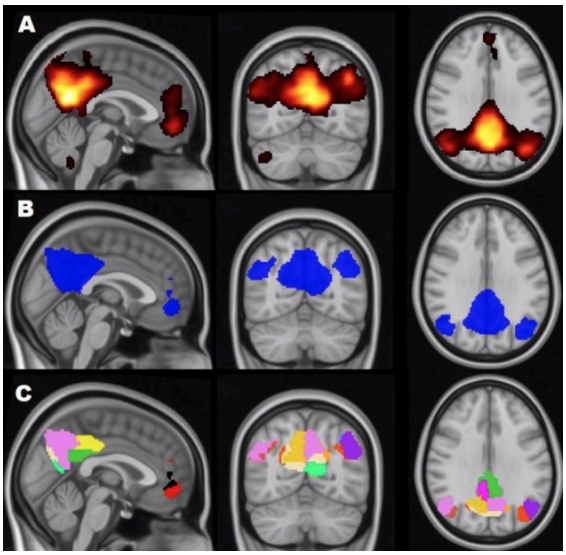

Note. Representation of the default mode network A. as the fourth component of the group independent component analysis output with dimensionality 25 (z-score range: 2.21 – 14.86), B. as mask with a z-score threshold of 4, C. after applying the default mode network mask to the automated anatomical labeling 3 atlas, containing 38 regions-of-interest included for analysis.

Network connectivity strength analysis

Dual regression was performed to obtain patient-specific spatial maps of the DMN component obtained with ICA (Beckmann et al., 2009). Normalized parameter estimates (i.e., z-scores) from the patient-specific DMN component were extracted from the dual regression output. The DMN mask was applied to the normalized parameter estimates spatial maps, after which mean z-scores were calculated for the baseline and postictal image of each patient. The mean z-score serves as a measure for network strength or network connectivity coherence, and was used as one of the outcome measures in our study (Mostert et al., 2016; Santhanam et al., 2019; Shumskaya et al., 2017).

Graph construction

The mask was applied to the Automated Anatomical Labeling atlas 3 for parcellation, which resulted in the DMN consisting of 38 nodes (Figure 1C) (Rolls et al., 2020; Tzourio-Mazoyer et al., 2002). The names and abbreviations of the nodes are listed in Appendix B. The mean time-series over all voxels were extracted for each node in all images. These time-series were used to estimate the partial correlation (PC) matrix for each image, containing the PCs for every node pair. The PC analysis was based on the method from Salvador et al. (2005), except that all node pairs with a mean negative PC were removed prior to the one-sample t-test as network-specific measures cannot be calculated with negative weights (Rubinov & Sporns, 2010). Correction for multiple comparisons was performed on the one-sample t-test output of the remaining node pairs using false discovery rate (FDR), taking into account the lack of independence between tests (Benjamini & Hochberg, 1995; Benjamini & Yekutieli, 2001).

This resulted in 74 significant ($p < 0.05$) node pairs (Appendix C & D). From a significant mean positive PC, there may still be a negative PC amongst all matrices. Therefore, the amount of PCs from the matrix with least positive significant PCs ($n = 63$) was divided by the total amount of edges ($n = 703$) to obtain a sparsity threshold value of 8.96%. This threshold was then applied to obtain the 63 highest significant PCs of each image. These formed a weighted undirected graph for each image, in which the PCs defined the weight of each edge. The sparsity threshold was used in order to preserve equal network degree across all images (van Wijk et al., 2010).

Graph analysis

Graph theoretical measures were calculated from each weighted undirected graph. Graph measures can be used to describe important topological properties of a particular network and have been used to reveal network connectivity abnormalities when comparing functional networks on different timepoints or between populations (Bullmore & Sporns, 2009; Rubinov & Sporns, 2010; Wang et al., 2010). The Brain Connectivity Toolbox was used to calculate two global network graph measures: mean clustering coefficient and characteristic path length (Rubinov & Sporns, 2010). These two measures indicate whether a network possesses a 'small-world' topology, which is associated with efficient information segregation and integration, respectively (Watts & Strogatz, 1998). The mean clustering coefficient reflects how adjacent nodes tend to cluster together, which was computed by averaging the amount of triangles around each node in the network (Rubinov & Sporns, 2010; Watts & Strogatz, 1998). The mean characteristic path length was computed by taking the average of shortest path length over each possible pair of vertices in the network (Rubinov & Sporns, 2010; Salvador et al., 2005; Schreiber, 2013; Watts & Strogatz, 1998). A network with a short path length needs fewer steps to reach a different node compared to a network with a long path length, and thus integrate information more efficiently. To examine small-world networks, the normalized clustering coefficient (γ = Cwreal / Cwrand), and the normalized characteristic path length (λ = Lwreal / Lwrand) were calculated (Humphries et al., 2006; Tian et al., 2011; Watts & Strogatz, 1998). Cwreal and Lwreal represent the clustering coefficient and characteristic path length from the networks of the baseline and postictal image of each patient. Cwrand and Lwrand represent the average clustering coefficient and characteristic path length derived from 1000 matched random networks which preserved degree-, weight- and strength-distributions (Rubinov & Sporns, 2010). A small-world network should meet the following criteria: $\gamma > 1$ and $\lambda \approx 1$, or $\sigma = \gamma / \lambda > 1$ with σ being small-worldness (Humphries et al., 2006; Tian et al., 2011; Watts & Strogatz, 1998). For a schematic overview of the analysis pipeline see Figure 2.

Figure 2

Analysis pipeline

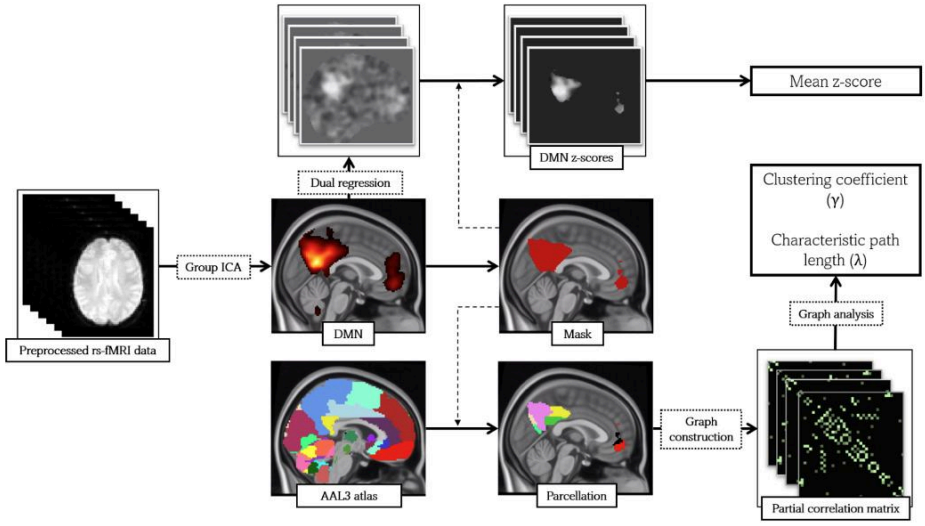

Note. Schematic representation of analysis pipeline. Rs-fMRI: functional magnetic resonance imaging; ICA: Independent Component Analysis; AAL3: Automated Anatomical Labeling 3; DMN: default mode network.

Statistical analysis

In order to determine whether there were significant differences between the baseline and postictal condition, a paired samples t-test was performed for the mean z-score, clustering coefficient, and characteristic path length. The association of both seizure duration and the timespan between the ECT-seizure and rs-fMRI acquisition with each network parameter was determined by performing an analysis of covariance (ANCOVA) with the difference between baseline and postictal images of each network parameter as dependent variable, while correcting for the type of study intervention as potential confounder. A p-value < 0.05 was considered a significant difference or association.

Results

Participants

We initially included twenty patients, from which two patients were excluded because the average FD was higher than 0.6 mm (n = 1) and the maximum FD was higher than 2 mm (n = 1). Both patient and ECT-characteristics are described in Table 1.

Table 1

Descriptive Statistics

Patients	N (%)	Mean (± SD)
Age		57.2 (± 13.9)
Gender		
Female	10 (55.6)	
Male	8 (44.4)	
ECT		
Electrode placement		
Unilateral	8 (44.4)	
Bilateral	10 (55.6)	
Midazolam		
Yes	5 (27.8)	
No	13 (72.2)	
Charge (milliCoulomb)		345.7 (± 163.1)
Seizure duration (seconds)		57.5 (± 22.2)
Time between ECT and rs-fMRI scan (minutes)		79.7 (± 9.5)

Note. *SD: Standard deviation; ECT: Electroconvulsive therapy; rs-fMRI: resting-state functional magnetic resonance imaging.*

Postictal alterations in DMN connectivity

The outcomes of the mean connectivity strength, clustering coefficient and characteristic path length are displayed in Figure 3. We compared the results of both graph measures at baseline to the postictal state using paired sample t-tests.

Mean network connectivity strength has been calculated by averaging the normalized parameter estimates (z-scores) within the DMN mask from the dual regression output of the DMN component. The mean z-score of the DMN was 3.98 (± 0.60) at baseline and 3.83 (± 0.72) after ECT, from which the difference was not significant (paired samples t-test, p = 0.51, Figure 3A).

Both baseline (1.68 ± 0.39) and postictal (1.38 ± 0.41) clustering coefficient fulfilled the small-world network criterium of $\gamma > 1$, and both baseline (1.00 ± 0.08) and postictal (0.97 ± 0.13) characteristic path length fulfilled it for $\lambda \approx 1$. DMN clustering coefficient was significantly decreased in the postictal state compared to baseline (paired samples t-test, p = 0.032, Figure 3B), whereas this was not the case for the characteristic path length (paired samples t-test, p = 0.57, Figure 3C).

Association with seizure duration

The ANCOVA revealed a positive association between seizure duration and the difference in clustering coefficient compared to baseline ($F(1, 13) = 5.14$, $p = 0.041$) (Figure 4A). There was also a negative association between seizure duration and the difference in characteristic path length compared to baseline ($F(1, 13) = 0.72$, $p = 0.019$) (Figure 4B). No association was found between seizure duration and the difference in mean connectivity strength compared to baseline ($F(1, 13) = 0.16$, $p = 0.70$).

Figure 3

Network measures boxplots

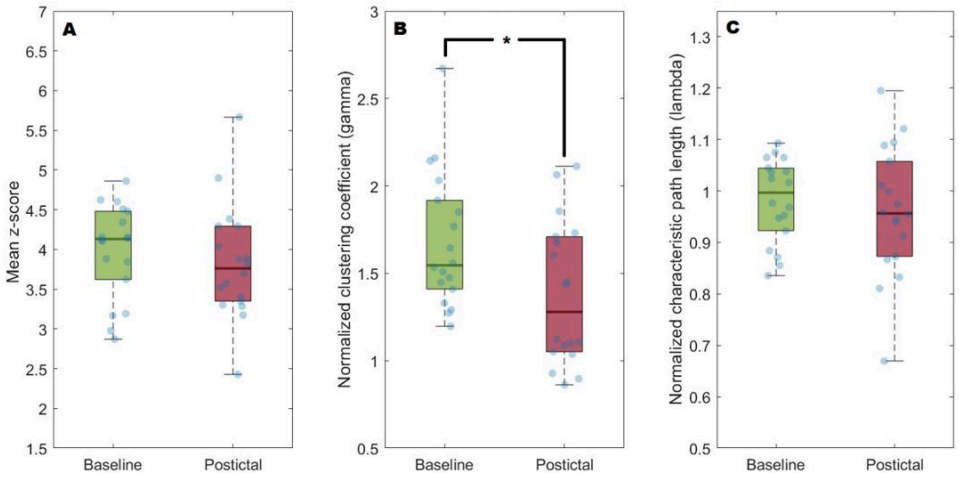

Note. Network measures at baseline and in the postictal state. A. Mean normalized parameter estimates (mean z-scores). B. Normalized clustering coefficient (γ = Cwreal / Cwrand). C. Normalized characteristic path length (λ=Lwreal/Lwrand). * paired samples t-test, $p < 0.05$

Figure 4

Association between both normalized clustering coefficient and normalized characteristic path length on seizure duration

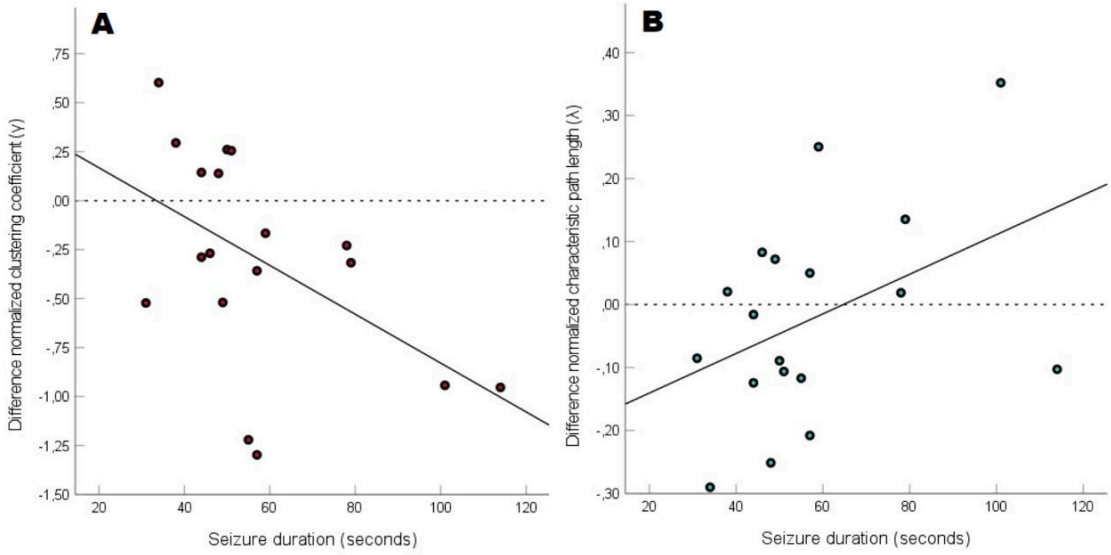

Note. Regression plots with line of best fit (solid line). The plots depict the association between seizure duration and the difference in A. normalized clustering coefficient compared to baseline and B. normalized characteristic path length compared to baseline.

Time between ECT and rs-fMRI

The time between the ECT-induced seizure and rs-fMRI acquisition was negatively associated with the difference in characteristic path length ($F(1, 13) = 7.96$, $p = 0.014$) compared to baseline (Figure 5), whereas this was not the case for mean connectivity strength ($F(1, 13) = 0.10$, $p = 0.76$) the clustering coefficient ($F(1, 13) = 1.38$, $p = 0.26$).

Figure 5

Association between normalized characteristic path length and time between ECT and rs-fMRI

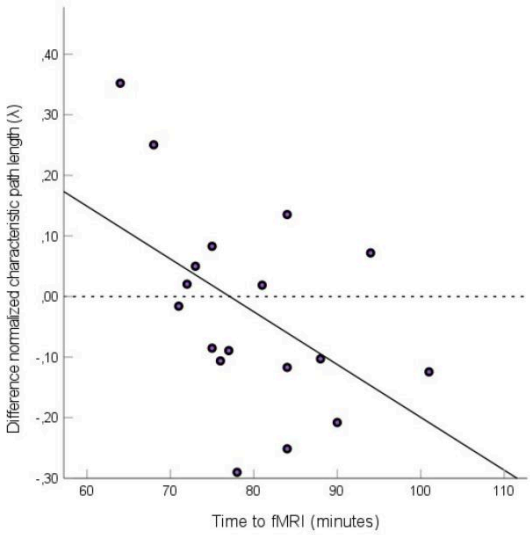

Note. Regression plots with line of best fit (solid line). The plots depict the association of the time between ECT and rs-fMRI on the difference in characteristic path length compared to baseline.

Discussion

To the best of our knowledge, this has been the first study to investigate the postictal state using rs-fMRI. We investigated alterations in DMN connectivity in the postictal state, and expected a postictal decrease in connectivity strength, segregation and integration compared to baseline. We identified a significant decrease in clustering coefficient in the postictal state compared to baseline. No difference was found in the mean connectivity strength, as well as the characteristic path length of the DMN. The difference in both clustering coefficient and characteristic path length compared to baseline were associated by seizure duration. In addition, the difference in characteristic path length compared to baseline was negatively associated with the duration between ECT and fMRI. Our findings suggest that alterations in functional topology of the DMN (i.e., network segregation and integration) may indicate pathological mechanisms of the postictal state.

DMN segregation and postictal symptoms

We observed a postictal decrease in clustering coefficient, which may be associated with the presence of several postictal clinical symptoms such as unconsciousness and cognitive impairments, which frequently occur after seizures (Pottkämper et al., 2020). A decreased clustering coefficient in the DMN may be related to postictal unconsciousness as comatose patients had a decreased clustering coefficient in the whole brain, as well as in the medial frontal

and posterior cingulate cortex, which are both part of the DMN (Crone et al., 2020).

Furthermore, postictal cognitive impairments may also be related to less DMN segregation, because a decrease in clustering coefficient in the DMN was associated with higher cognitive impairments in epilepsy and obstructive sleep apnea patients (Chen et al., 2018; Khalife et al., 2022). A similar association was observed in carotid stenosis and ischemic stroke patients, in which a lower clustering coefficient in the whole brain was associated with higher cognitive impairments (Chang et al., 2016; Li et al., 2021). Thus, decreased DMN segregation may be associated with postictal clinical symptoms.

Underlying physiology

The physiological mechanism underlying a decrease in clustering coefficient remains largely unknown. One explanation for a decreased clustering coefficient may be related to local hypoperfusion in critical network hubs. Previous studies showed that brain hub regions (i.e., highly connected nodes within a network) show higher metabolic requirements, as they are associated with both a higher CBF and glucose metabolism (Hagmann et al., 2008; Liang et al., 2013a; Tomasi et al., 2013; Várkuti et al., 2011). Hub regions are known to contribute to the creation of local clusters called modules, which have dense interconnectivity and few connections with nodes in other modules, leading to an increased whole network information flow (Farahani et al., 2019). Therefore, the higher metabolic demands of hub regions may be required to efficiently orchestrate the network as a whole (Hagmann et al., 2008; Liao et al., 2017). The vasoconstriction-mediated hypoperfusion hypothesis suggests a reduction in CBF in seizure onset zones during the first hour after seizures, causing a diminished postictal metabolic supply in several brain regions (Farrell et al., 2016, 2017). A reduction of CBF was measured in the early postictal state in specific cortical regions belonging to the DMN, supporting their involvement in the postictal state (Blumenfeld et al., 2009). Therefore, the decreased DMN segregation may be driven by local postictal hypoperfusion, preventing hub regions to successfully form local clusters.

Seizure duration

We observed that longer seizures were associated with a stronger postictal decrease in clustering coefficient and a stronger postictal increase in characteristic path length compared to baseline. Thus, DMN topology is disrupted more severely in network segregation and integration as a result of longer seizures.

Disruption of network segregation and integration may reflect the severity of the postictal state. Longer seizures were found to be associated with a longer duration and more severe symptomatology of the postictal state (Krauss & Edwards, 2014; Ohira et al., 2019). Additionally, longer seizures were positively correlated with more postictal hypoperfusion and hypoxia in both rodents and humans, which in rodents was associated with behavioral dysfunctions related to postictal symptoms (Farrell et al., 2016, 2017). Thus, disruption of network segregation and integration, as well as the severity of postictal symptoms seem to be associated with seizure duration, suggesting that disruption in DMN segregation and integration may reflect the severity of the postictal state.

Time between ECT and rs-MRI acquisition

We observed a negative association between the time between ECT and rs-fMRI acquisition and the change in characteristic path length compared to baseline. Patients who were scanned earliest after the ECT-induced seizure (i.e., 64 minutes) had a higher characteristic path length compared to patients whose rs-fMRI were performed at a later stage (i.e., 101 minutes). Thus, the time between the seizure and rs-fMRI acquisition may have been too long to observe postictal differences in characteristic path length. This may suggest that DMN integration is diminished only in the early postictal state, though some patients may also have been scanned too late for postictal effects of integration to be measurable.

The decrease in DMN segregation, however, was not associated with time between ECT and rs-fMRI. An explanations for this may be that alterations in gray and white matter connectivity have distinct influences on postictal changes in functional network segregation and integration. White matter connectivity has been suggested to cause dynamic changes in functional topological organization at a temporal scale of seconds to minutes (Liao et al., 2015; Shen et al., 2015). This suggests that these changes may also not have been captured due to the time between ECT and rs-fMRI acquisition, and may therefore relate to DMN integration.

Mean connectivity strength

We expected a postictal decrease in mean connectivity strength of the DMN as this has been found in patients with symptoms comparable to the postictal state (Crone et al., 2011; Demertzi et al., 2014; Garcés et al., 2014; Norton et al., 2012; Taïb et al., 2023; Vanhaudenhuyse et al., 2010). Changes in mean connectivity strength in the DMN may not have been captured as changes in connectivity may occur very local. The vasoconstriction-mediated hypoperfusion theory hypothesizes that local decreases in CBF are present in seizure onset zones during the first hour after seizures (Farrell et al., 2016, 2017). Functional connectivity is tightly coupled with CBF (Liang et al., 2013b). Therefore, local postictal hypoperfusion may cause a local decrease in functional connectivity that is too small to detect widespread decreases in mean connectivity strength.

Future directions

The present study assessed postictal topological alterations in the DMN using global graph measures. One interesting possibility for future research is doing a more extensive graph analysis within the postictal DMN using nodal graph measures. This type of analysis could identify whether specific hub-regions of the DMN may be disrupted during the postictal state (Liao et al., 2017; Rubinov & Sporns, 2010). An additional interesting approach would be to test if the function of these hub regions is related to postictal hypoperfusion, as measured by arterial spin labeling MRI. As the time between the ECT-induced seizure and rs-fMRI seems to be associated with the difference in characteristic path length compared to baseline, it may also be the case for nodal graph measures. Therefore, results should be controlled for the duration between seizure and rs-fMRI.

Future studies may also use a measure for assessing the type of postictal symptoms, as well as the severity of the postictal state in order to close the gap between alterations in graph measures and their relation to clinical manifestations. Furthermore, this could shed more light on the relation between seizure duration and the duration, severity or symptomatology of the postictal state.

Limitations

Several limitations in the present study should be addressed. First, the sample size in this study is small, reducing statistical power and increasing the probability of type II errors (Shreffler & Huecker, 2022). It also limits the possibilities for using nodal graph measures, as these findings must be corrected for multiple comparisons over all nodes in order to prevent increased probability of type I errors (Shreffler & Huecker, 2022).

Second, postictal alterations in connectivity may be overlooked due to the long time between ECT and rs-fMRI acquisition, which was caused by postictal practical challenges. Patients often woke up confused and restless in the first minutes after ECT and had to be monitored until they were stable enough to be transported to the radiological department. The increased likelihood of movement may have further influenced imaging quality and caused bias, even though extensive motion-correction and quality checks have been performed (Alexander-Bloch et al., 2016).

Third, five patients received midazolam after ECT due to postictal delirium. The postictal administration of midazolam may have contributed to a decrease in DMN segregation or integration, as sedation by midazolam has been showed to decrease functional DMN connectivity (Greicius et al., 2008). Midazolam has a half-life of 1.5-2.5 hours, suggesting that there may still have been residues in the blood stream at the time of scanning (Lingamchetty et al., 2022).

Fourth, the nodes that we used differed in size, potentially causing bias in the graph analysis. We applied the DMN mask to the Automated Anatomical Labeling 3 atlas to obtain nodes specific to the DMN (Rolls et al., 2020). As a result, nodes located at the edge of the mask decreased in size, whereas this was not the case for centrally located nodes. Altered time-series in voxels located in small nodes may therefore have had a disproportionate impact on the graph analysis compared to large nodes.

Fifth, resting-state functional connectivity in the DMN is known to be altered in MDD patients (Mulders et al., 2015). Differences in baseline DMN connectivity may have affected each patient's response to the ECT-induced seizure, thereby potentially confounding the difference in DMN connectivity between baseline and the postictal state.

Lastly, only properties of the DMN have been analyzed in the present study, thereby potentially missing effects of other networks that may further elucidate mechanisms of the postictal state. The salience and central-executive network, for instance, are supposed to interact with the DMN and may play a role in cognition and may therefore be altered in the postictal state (Chand et al., 2017; Chand & Dhamala, 2016). Furthermore, our findings may generalize to the entire brain, instead of being DMN-specific.

Conclusion

We established disrupted functional connectivity of the DMN in the postictal state. Information segregation in the DMN decreased postictally, while network connectivity strength and information integration do not seem to be affected. Longer seizures are associated with a stronger postictal decrease in DMN segregation and integration. In addition, the time between seizure and rs-fMRI acquisition seems to be of importance for measuring postictal changes in DMN integration. Our findings provide an improved understanding of the pathological mechanisms underlying the postictal state, which may eventually help elucidate targets for new modes of treatment.

References

Alexander-Bloch, A., Clasen, L., Stockman, M., Ronan, L., Lalonde, F., Giedd, J., & Raznahan, A. (2016). Subtle In-Scanner Motion Biases Automated Measurement of Brain Anatomy From In Vivo MRI. https://doi.org/10.1002/hbm.23180

Andersson, J. L. R., Skare, S., & Ashburner, J. (2003). How to correct susceptibility distortions in spin-echo echo-planar images: Application to diffusion tensor imaging. NeuroImage, 20(2), 870–888. https://doi.org/10.1016/S1053-8119(03)00336-7

Avants, B. B., Epstein, C. L., Grossman, M., & Gee, J. C. (2008). Symmetric diffeomorphic image registration with cross-correlation: Evaluating automated labeling of elderly and neurodegenerative brain. Medical Image Analysis, 12(1), 26–41. https://doi.org/10.1016/j.media.2007.06.004

Beckmann, C. F., DeLuca, M., Devlin, J. T., & Smith, S. M. (2005). Investigations into resting-state connectivity using independent component analysis. Philosophical Transactions of the Royal Society B: Biological Sciences, 360(1457), 1001. https://doi.org/10.1098/RSTB.2005.1634

Beckmann, C. F., & Smith, S. M. (2004). Probabilistic Independent Component Analysis for Functional Magnetic Resonance Imaging. IEEE Transactions on Medical Imaging, 23(2), 137–152. https://doi.org/10.1109/TMI.2003.822821

Beckmann, C., Mackay, C., Filippini, N., & Smith, S. (2009). Group comparison of resting-state FMRI data using multi-subject ICA and dual regression. NeuroImage, 47, S148. https://doi.org/10.1016/S1053-8119(09)71511-3

Behzadi, Y., Restom, K., Liau, J., & Liu, T. T. (2007). A component based noise correction method (CompCor) for BOLD and perfusion based fMRI. NeuroImage, 37(1), 90–101. https://doi.org/10.1016/j.neuroimage.2007.04.042

Benjamini, Y., & Hochberg, Y. (1995). Controlling the False Discovery Rate: A Practical and Powerful Approach to Multiple Testing. Source: Journal of the Royal Statistical Society. Series B (Methodological), 57(1), 289–300.

Benjamini, Y., & Yekutieli, D. (2001). THE CONTROL OF THE FALSE DISCOVERY RATE IN MULTIPLE TESTING UNDER DEPENDENCY. In The Annals of Statistics (Vol. 29, Issue 4).

Blumenfeld, H., Varghese, G. I., Purcaro, M. J., Motelow, J. E., Enev, M., McNally, K. A., Levin, A. R., Hirsch, L. J., Tikofsky, R., Zubal, I. G., Paige, A. L., & Spencer, S. S. (2009). Cortical and subcortical networks in human secondarily generalized tonicclonic seizures. Brain, 132(4), 999–1012. https://doi.org/10.1093/brain/awp028

Broek, W. W. van den (Walter W., & Richtlijncommissie elektroconvulsietherapie. (2010). Richtlijn elektroconvulsietherapie. De Tijdstroom.

Broyd, S. J., Demanuele, C., Debener, S., Helps, S. K., James, C. J., & Sonuga-Barke, E. J. S. (2009). Default-mode brain dysfunction in mental disorders: A systematic review. In Neuroscience and Biobehavioral Reviews (Vol. 33, Issue 3, pp. 279–296). https://doi.org/10.1016/j.neubiorev.2008.09.002

Bullmore, E., & Sporns, O. (2009). Complex brain networks: graph theoretical analysis of structural and functional systems. Nature Reviews Neuroscience 2009 10:3, 10(3), 186–198. https://doi.org/10.1038/nrn2575

Chand, G. B., & Dhamala, M. (2016). Interactions among the Brain Default-Mode, Salience, and Central-Executive Networks during Perceptual Decision-Making of Moving Dots. Brain Connectivity, 6(3), 249–254. https://doi.org/10.1089/BRAIN.2015.0379/SUPPL_FILE/SUPP_FIGURE5.PDF

Chand, G. B., Wu, J., Hajjar, I., & Qiu, D. (2017). Interactions of the Salience Network and Its Subsystems with the Default-Mode and the Central-Executive Networks in Normal Aging and Mild Cognitive Impairment. Brain Connectivity, 7(7), 401. https://doi.org/10.1089/BRAIN.2017.0509

Chang, T.-Y., Huang, K.-L., Ho, M.-Y., Ho, P.-S., Chang, C.-H., Liu, C.-H., Chang, Y.-J., Wong, H.-F., Hsieh, I.-C., Lee, T.-H., & Liu, H.-L. (2016). Graph theoretical analysis of functional networks and its relationship to cognitive decline in patients with carotid stenosis. Journal of Cerebral Blood Flow & Metabolism, 36(4), 808–818. https://doi.org/10.1177/0271678X15608390

Chen, L., Fan, X., Li, H., Ye, C., Yu, H., Gong, H., Zeng, X., Peng, D., & Yan, L. (2018). Topological reorganization of the default mode network in severe male obstructive sleep apnea. Frontiers in Neurology, 9(JUN). https://doi.org/10.3389/fneur.2018.00363

Crone, J. S., Ladurner, G., Höller, Y., Golaszewski, S., Trinka, E., & Kronbichler, M. (2011). Deactivation of the Default Mode Network as a Marker of Impaired Consciousness: An fMRI Study. PLoS ONE, 6(10). https://doi.org/10.1371/JOURNAL.PONE.0026373

Crone, J. S., Lutkenhoff, E. S., Vespa, P. M., & Monti, M. M. (2020). A systematic investigation of the association between network dynamics in the human brain and the state of consciousness. Neuroscience of Consciousness, 6(1). https://doi.org/10.1093/nc/niaa008

Crone, J. S., Schurz, M., Höller, Y., Bergmann, J., Monti, M., Schmid, E., Trinka, E., & Kronbichler, M. (2015). Impaired consciousness is linked to changes in effective connectivity of the posterior cingulate cortex within the default mode network. Neuroimage, 110, 101. https://doi.org/10.1016/J.NEUROIMAGE.2015.01.037

de Boer, H. M. (2014). Epilepsy; Social Consequences. Encyclopedia of the Neurological Sciences, 157–163. https://doi.org/10.1016/B978-0-12-385157-4.00292-X

d'Elia, G. (1970). Unilateral Electroconvulsive Therapy. Acta Psychiatrica Scandinavica.

Demertzi, A., Gómez, F., Crone, J. S., Vanhaudenhuyse, A., Tshibanda, L., Noirhomme, Q., Thonnard, M., Charland-Verville, V., Kirsch, M., Laureys, S., & Soddu, A. (2014). Multiple fMRI system-level baseline connectivity is disrupted in patients with consciousness alterations. Cortex; a Journal Devoted to the Study of the Nervous System and Behavior, 52(1), 35–46. https://doi.org/10.1016/J.CORTEX.2013.11.005

Esteban, O., Markiewicz, C. J., Goncalves, M., Provins, C., Kent, J. D., DuPre, E., Salo, T., Ciric, R., Pinsard, B., Blair, R. W., Poldrack, R. A., & Gorgolewski, K. J. (2018). fMRIPrep: a robust preprocessing pipeline for functional MRI. https://doi.org/10.5281/ZENODO.7117719

Evans, A. C., Janke, A. L., Collins, D. L., & Baillet, S. (2012). Brain templates and atlases. NeuroImage, 62(2), 911–922. https://doi.org/10.1016/J.NEUROIMAGE.2012.01.024

Farahani, F. v., Karwowski, W., & Lighthall, N. R. (2019). Application of Graph Theory for Identifying Connectivity Patterns in Human Brain Networks: A Systematic Review. Frontiers in Neuroscience, 13(JUN). https://doi.org/10.3389/FNINS.2019.00585

Farrell, J. S., Colangeli, R., Wolff, M. D., Wall, A. K., Phillips, T. J., George, A., Federico, P., & Teskey, G. C. (2017). Postictal hypoperfusion/hypoxia provides the foundation for a unified theory of seizure-induced brain abnormalities and behavioral dysfunction. In Epilepsia (Vol. 58, Issue 9, pp. 1493–1501). Blackwell Publishing Inc. https://doi.org/10.1111/epi.13827

Farrell, J. S., Gaxiola-Valdez, I., Wolff, M. D., David, L. S., Dika, H. I., Geeraert, B. L., Wang, X. R., Singh, S., Spanswick, S. C., Dunn, J. F., Antle, M. C., Federico, P., & Teskey, G. C. (2016). Postictal behavioural impairments are due to a severe prolonged hypoperfusion/hypoxia event that is COX-2 dependent. ELife, 5(NOVEMBER2016). https://doi.org/10.7554/ELIFE.19352

Fisher, R. S., & Schachter, S. C. (2000). The Postictal State: A Neglected Entity in the Management of Epilepsy. Epilepsy and Behavior, 1(1), 52–59. https://doi.org/10.1006/EBEH.2000.0023

Fonov, V., Evans, A., McKinstry, R., Almli, C., & Collins, D. (2009). Unbiased nonlinear average age-appropriate brain templates from birth to adulthood. NeuroImage, 47, S102. https://doi.org/10.1016/S1053-8119(09)70884-5

Garcés, P., Ángel Pineda-Pardo, J., Canuet, L., Aurtenetxe, S., López, M. E., Marcos, A., Yus, M., Llanero-Luque, M., Del-Pozo, F., Sancho, M., & Maestú, F. (2014). The Default Mode Network is functionally and structurally disrupted in amnestic mild cognitive impairment — A bimodal MEG–DTI study. NeuroImage: Clinical, 6, 214–221. https://doi.org/10.1016/J.NICL.2014.09.004

Gorgolewski, K., Burns, C. D., Madison, C., Clark, D., Halchenko, Y. O., Waskom, M. L., & Ghosh, S. S. (2011). Nipype: A flexible, lightweight and extensible neuroimaging data processing framework in Python. Frontiers in Neuroinformatics, 5. https://doi.org/10.3389/fninf.2011.00013

Gotman, J., Grova, C., Bagshaw, A., Kobayashi, E., Aghakhani, Y., & Dubeau, F. (2005). Generalized epileptic discharges show thalamocortical activation and suspension of the default state of the brain (Vol. 102, Issue 42). www.pnas.orgcgidoi10.1073pnas.0504935102

Greicius, M. D., Kiviniemi, V., Tervonen, O., Vainionpää, V., Alahuhta, S., Reiss, A. L., & Menon, V. (n.d.). Persistent Default-Mode Network Connectivity During Light Sedation. https://doi.org/10.1002/hbm.20537

Greve, D. N., & Fischl, B. (2009). Accurate and robust brain image alignment using boundary-based registration. NeuroImage, 48(1), 63–72. https://doi.org/10.1016/j.neuroimage.2009.06.060

Hagmann, P., Cammoun, L., Gigandet, X., Meuli, R., Honey, C. J., van Wedeen, J., & Sporns, O. (2008). Mapping the Structural Core of Human Cerebral Cortex. PLoS Biology, 6(7), 1479–1493. https://doi.org/10.1371/JOURNAL.PBIO.0060159

Humphries, M. D., Gurney, K., & Prescott, T. J. (n.d.). The brainstem reticular formation is a small-world, not scale-free, network. https://doi.org/10.1098/rspb.2005.3354

Hyvärinen, A. (1999). Fast and Robust Fixed-Point Algorithms for Independent Component Analysis. IEEE TRANSACTIONS ON NEURAL NETWORKS, 10(3).

Jenkinson, M., Bannister, P., Brady, M., & Smith, S. (2002). Improved Optimization for the Robust and Accurate Linear Registration and Motion Correction of Brain Images. NeuroImage, 17(2), 825–841. https://doi.org/10.1006/nimg.2002.1132

Jenkinson, M., & Smith, S. (2001). A global optimisation method for robust affine registration of brain images. Medical Image Analysis, 5(2), 143–156. https://doi.org/10.1016/S1361-8415(01)00036-6

Khalife, M. R., Scott, R. C., & Hernan, A. E. (2022). Mechanisms for Cognitive Impairment in Epilepsy: Moving Beyond Seizures. Frontiers in Neurology, 13. https://doi.org/10.3389/FNEUR.2022.878991

Krauss, G. L., & Edwards, H. B. (2014). Postictal Manifestations. Encyclopedia of the Neurological Sciences, 953–955. https://doi.org/10.1016/B978-0-12-385157-4.00301-8

Kropotov, J. D. (2016). Electroconvulsive Therapy. Functional Neuromarkers for Psychiatry, 267–271. https://doi.org/10.1016/B978-0-12-410513-3.00017-6

Lanczos, C. (1964). Evaluation of Noisy Data. Journal of the Society for Industrial and Applied Mathematics Series B Numerical Analysis, 1(1), 76–85. https://doi.org/10.1137/0701007

Laufs, H. (2012). Functional imaging of seizures and epilepsy: Evolution from zones to networks.

In Current Opinion in Neurology (Vol. 25, Issue 2, pp. 194–200). https://doi.org/10.1097/WCO.0b013e3283515db9

Laufs, H., Hamandi, K., Salek-Haddadi, A., Kleinschmidt, A. K., Duncan, J. S., & Lemieux, L. (2007). Temporal lobe interictal epileptic discharges affect cerebral activity in "default mode" brain regions. Human Brain Mapping, 28(10), 1023–1032. https://doi.org/10.1002/HBM.20323

Li, Y., Yu, Z., Wu, P., & Chen, J. (2021). The disrupted topological properties of structural networks showed recovery in ischemic stroke patients: a longitudinal design study. BMC Neuroscience, 22(1). https://doi.org/10.1186/s12868-021-00652-1

Liang, X., Zou, Q., He, Y., & Yang, Y. (2013a). Coupling of functional connectivity and regional cerebral blood flow reveals a physiological basis for network hubs of the human brain. Proceedings of the National Academy of Sciences of the United States of America, 110(5), 1929–1934. https://doi.org/10.1073/PNAS.1214900110

Liang, X., Zou, Q., He, Y., & Yang, Y. (2013b). Coupling of functional connectivity and regional cerebral blood flow reveals a physiological basis for network hubs of the human brain. Proceedings of the National Academy of Sciences of the United States of America, 110(5), 1929–1934. https://doi.org/10.1073/PNAS.1214900110/SUPPL_FILE/PNAS.201214900SI.PDF

Liao, X., Vasilakos, A. v., & He, Y. (2017). Small-world human brain networks: Perspectives and challenges. Neuroscience and Biobehavioral Reviews, 77, 286–300. https://doi.org/10.1016/J.NEUBIOREV.2017.03.018

Liao, X., Yuan, L., Zhao, T., Dai, Z., Shu, N., Xia, M., Yang, Y., Evans, A., & He, Y. (2015). Spontaneous functional network dynamics and associated structural substrates in the human brain. Frontiers in Human Neuroscience, 9(september), 1–17. https://doi.org/10.3389/FNHUM.2015.00478/BIBTEX

Lingamchetty, T. N., Hosseini, S. A., & Saadabadi, A. (2022). Midazolam. XPharm: The Comprehensive Pharmacology Reference, 1–5. https://doi.org/10.1016/B978-008055232-3.62185-3

Lui, S., Ouyang, L., Chen, Q., Huang, X., Tang, H., Chen, H., Zhou, D., Kemp, G. J., & Gong, Q. (2008). Differential interictal activity of the precuneus/posterior cingulate cortex revealed by resting state functional MRI at 3T in generalized vs. partial seizure. Journal of Magnetic Resonance Imaging : JMRI, 27(6), 1214–1220. https://doi.org/10.1002/JMRI.21370

Manning, K. J., & Steffens, D. C. (2016). Systems Neuroscience in Late-Life Depression. Systems Neuroscience in Depression, 325–340. https://doi.org/10.1016/B978-0-12-802456-0.00011-X

McNally, K. A., & Blumenfeld, H. (2004). Focal network involvement in generalized seizures: New insights from electroconvulsive therapy. In Epilepsy and Behavior (Vol. 5, Issue 1, pp. 3–12). https://doi.org/10.1016/j.yebeh.2003.10.020

Mostert, J. C., Shumskaya, E., Mennes, M., Onnink, A. M. H., Hoogman, M., Kan, C. C., Arias Vasquez, A., Buitelaar, J., Franke, B., & Norris, D. G. (2016). Characterising resting-state functional connectivity in a large sample of adults with ADHD. Progress in Neuro-Psychopharmacology and Biological Psychiatry, 67, 82–91. https://doi.org/10.1016/J.PNPBP.2016.01.011

Mulders, P. C., van Eijndhoven, P. F., Schene, A. H., Beckmann, C. F., & Tendolkar, I. (2015). Resting-state functional connectivity in major depressive disorder: A review. Neuroscience and Biobehavioral Reviews, 56, 330–344. https://doi.org/10.1016/J.NEUBIOREV.2015.07.014

Murray, E. D., Buttner, E. A., & Price, B. H. (2012). Depression and Psychosis in Neurological Practice. Neurology in Clinical Practice, 92–116. https://doi.org/10.1016/B978-1-4377-0434-1.00009-8

Norton, L., Hutchison, R. M., Young, G. B., Lee, D. H., Sharpe, M. D., & Mirsattari, S. M. (2012). Disruptions of functional connectivity in the default mode network of comatose patients. Neurology, 78(3), 175–181. https://doi.org/10.1212/WNL.0B013E31823FCD61

Ohira, J., Yoshimura, H., Morimoto, T., Ariyoshi, K., & Kohara, N. (2019). Factors associated with the duration of the postictal state after a generalized convulsion. Seizure, 65, 101–105. https://doi.org/10.1016/J.SEIZURE.2019.01.001

Pottkämper, J. C. M., Hofmeijer, J., van Waarde, J. A., & van Putten, M. J. A. M. (2020). The postictal state — What do we know? In Epilepsia (Vol. 61, Issue 6, pp. 1045–1061). Blackwell Publishing Inc. https://doi.org/10.1111/epi.16519

Pottkämper, J. C. M., Verdijk, J. P. A. J., Hofmeijer, J., van Waarde, J. A., & van Putten, M. J. A. M. (2021). Seizures induced in electroconvulsive therapy as a human epilepsy model: A comparative case study. Epilepsia Open, 6(4), 672–684. https://doi.org/10.1002/epi4.12532

Power, J. D., Mitra, A., Laumann, T. O., Snyder, A. Z., Schlaggar, B. L., & Petersen, S. E. (2014). Methods to detect, characterize, and remove motion artifact in resting state fMRI. NeuroImage, 84, 320–341. https://doi.org/10.1016/j.neuroimage.2013.08.048

Pruim, R. H. R., Mennes, M., van Rooij, D., Llera, A., Buitelaar, J. K., & Beckmann, C. F. (2015). ICA-AROMA: A robust ICA-based strategy for removing motion artifacts from fMRI data. NeuroImage, 112, 267–277. https://doi.org/10.1016/j.neuroimage.2015.02.064

Raichle, M. E., MacLeod, A. M., Snyder, A. Z., Powers, W. J., Gusnard, D. A., & Shulman, G. L. (2001). A default mode of brain function. Proceedings of the National Academy of Sciences of the United States of America, 98(2), 676–682. https://doi.org/10.1073/PNAS.98.2.676/ASSET/0D756665-76C2-42A2-ACA7-01DE9C6DEDA4/ASSETS/GRAPHIC/PQ0115125005.JPEG

Rolls, E. T., Huang, C. C., Lin, C. P., Feng, J., & Joliot, M. (2020). Automated anatomical labelling atlas 3. NeuroImage, 206, 116189. https://doi.org/10.1016/J.NEUROIMAGE.2019.116189

Rubinov, M., & Sporns, O. (2010). Complex network measures of brain connectivity: Uses and interpretations. NeuroImage, 52(3), 1059–1069. https://doi.org/10.1016/.neuroimage.2009.10.003

Salvador, R., Suckling, J., Coleman, M. R., Pickard, J. D., Menon, D., & Bullmore, E. (2005). Neurophysiological architecture of functional magnetic resonance images of human brain. Cerebral Cortex (New York, N.Y.: 1991), 15(9), 1332–2342. https://doi.org/10.1093/CERCOR/BHI016

Santhanam, P., Wilson, S. H., Oakes, T. R., & Weaver, L. K. (2019). Effects of mild traumatic brain injury and post-traumatic stress disorder on resting-state default mode network connectivity. Brain Research, 1711, 77–82. https://doi.org/10.1016/J.BRAINRES.2019.01.015

Satterthwaite, T. D., Elliott, M. A., Gerraty, R. T., Ruparel, K., Loughead, J., Calkins, M. E., Eickhoff, S. B., Hakonarson, H., Gur, R. C., Gur, R. E., & Wolf, D. H. (2013). An improved framework for confound regression and filtering for control of motion artifact in the preprocessing of resting-state functional connectivity data. NeuroImage, 64(1), 240–256. https://doi.org/10.1016/j.neuroimage.2012.08.052

Schreiber, F. (2013). Characteristic Path Length. Encyclopedia of Systems Biology, 395–395. https://doi.org/10.1007/978-1-4419-9863-7_1460

Shen, K., Hutchison, R. M., Bezgin, G., Everling, S., & McIntosh, A. R. (2015). Network Structure Shapes Spontaneous Functional Connectivity Dynamics. The Journal of Neuroscience, 35(14), 5579. https://doi.org/10.1523/JNEUROSCI.4903-14.2015

Shreffler, J., & Huecker, M. R. (2022). Type I and Type II Errors and Statistical Power. StatPearls. https://www.ncbi.nlm.nih.gov/books/NBK557530/

Shumskaya, E., van Gerven, M. A. J., Norris, D. G., Vos, P. E., & Kessels, R. P. C. (2017). Abnormal connectivity in the sensorimotor network predicts attention deficits in traumatic brain injury. Experimental Brain Research, 235(3), 799–807. https://doi.org/10.1007/S00221-016-4841-Z/FIGURES/3

Stafstrom, C. E., & Carmant, L. (n.d.). Seizures and Epilepsy: An Overview for Neuroscientists. https://doi.org/10.1101/cshperspect.a022426

Steiger, B. K., & Jokeit, H. (2017). Why epilepsy challenges social life. Seizure, 44, 194–198. https://doi.org/10.1016/J.SEIZURE.2016.09.008

Taïb, S., Yrondi, A., Lemesle, B., Péran, P., & Pariente, J. (2023). What are the neural correlates of dissociative amnesia? A systematic review of the functional neuroimaging literature. Frontiers in Psychiatry, 14, 47. https://doi.org/10.3389/FPSYT.2023.1092826

Tian, L., Wang, J., Yan, C., & He, Y. (2011). Hemisphere- and gender-related differences in small-world brain networks: a resting-state functional MRI study. NeuroImage, 54(1), 191–202. https://doi.org/10.1016/J.NEUROIMAGE.2010.07.066

Tomasi, D., Wang, G. J., & Volkow, N. D. (2013). Energetic cost of brain functional connectivity. Proceedings of the National Academy of Sciences of the United States of America, 110(33), 13642–13647. https://doi.org/10.1073/PNAS.1303346110/SUPPL_FILE/PNAS.201303346SI.PDF

Tustison, N. J., Avants, B. B., Cook, P. A., Zheng, Y., Egan, A., Yushkevich, P. A., & Gee, J. C. (2010). N4ITK: Improved N3 bias correction. IEEE Transactions on Medical Imaging, 29(6), 1310–1320. https://doi.org/10.1109/TMI.2010.2046908

Tzourio-Mazoyer, N., Landeau, B., Papathanassiou, D., Crivello, F., Etard, O., Delcroix, N., Mazoyer, B., & Joliot, M. (2002). Automated Anatomical Labeling of Activations in SPM Using a Macroscopic Anatomical Parcellation of the MNI MRI Single-Subject Brain. NeuroImage, 15(1), 273–289. https://doi.org/10.1006/NIMG.2001.0978

van Wijk, B. C. M., Stam, C. J., & Daffertshofer, A. (2010). Comparing brain networks of different size and connectivity density using graph theory. PloS One, 5(10). https://doi.org/10.1371/JOURNAL.PONE.0013701

Vanhaudenhuyse, A., Noirhomme, Q., Tshibanda, L. J. F., Bruno, M. A., Boveroux, P., Schnakers, C., Soddu, A., Perlbarg, V., Ledoux, D., Brichant, J. F., Moonen, G., Maquet, P., Greicius, M. D., Laureys, S., & Boly, M. (2010). Default network connectivity reflects the level of consciousness in non-communicative brain-damaged patients. Brain, 133(1), 161. https://doi.org/10.1093/BRAIN/AWP313

Várkuti, B., Cavusoglu, M., Kullik, A., Schiffler, B., Veit, R., Yilmaz, Ö., Rosenstiel, W., Braun, C., Uludag, K., Birbaumer, N., & Sitaram, R. (2011). Quantifying the Link between Anatomical Connectivity, Gray Matter Volume and Regional Cerebral Blood Flow: An Integrative MRI Study. PLoS ONE, 6(4). https://doi.org/10.1371/JOURNAL.PONE.0014801

Wang, J., Zuo, X., & He, Y. (2010). Graph-based network analysis of resting-state functional MRI. Frontiers in Systems Neuroscience, 4, 16. https://doi.org/10.3389/FNSYS.2010.00016/BIBTEX

Watts, D. J., & Strogatz, S. H. (1998). Collective dynamics of 'small-world' networks. Nature 1998 393:6684, 393(6684), 440–442. https://doi.org/10.1038/30918

Wolff, M. D. (2020). Dynamic Oxygen Changes with Status Epilepticus, Seizures, and the Postictal State. http://hdl.handle.net/1880/112487

Zhang, Y., Brady, M., & Smith, S. (2001). Segmentation of brain MR images through a hidden Markov random field model and the expectation-maximization algorithm. IEEE Transactions on Medical Imaging, 20(1), 45–57. https://doi.org/10.1109/42.906424

Appendix A

Results included in this manuscript come from preprocessing performed using fMRIPrep 21.0.2 (Esteban et al., 2018; RRID:SCR_002502), which is based on Nipype 1.6.1 (Gorgolewski et al., 2011; RRID:SCR_002502).

Preprocessing of B0 inhomogeneity mappings

A total of 1 fieldmaps were found available within the input BIDS structure for this particular subject. A B0-nonuniformity map (or fieldmap) was estimated based on two (or more) echo-planar imaging (EPI) references with topup (Andersson et al., 2003; FSL 6.0.5.1:57b01774).

Anatomical data preprocessing

A total of 1 T1-weighted (T1w) images were found within the input BIDS dataset. The T1-weighted (T1w) image was corrected for intensity non-uniformity (INU) with N4BiasFieldCorrection (Tustison et al., 2010), distributed with ANTs 2.3.3 (Avants et al., 2008; RRID:SCR_004757), and used as T1w-reference throughout the workflow. The T1w-reference was then skull-stripped with a Nipype implementation of the antsBrainExtraction.sh workflow (from ANTs), using OASIS30ANTs as target template. Brain tissue segmentation of cerebrospinal fluid (CSF), white-matter (WM) and gray-matter (GM) was performed on the brain-extracted T1w using fast (Zhang et al., 2001; FSL 6.0.5.1:57b01774, RRID:SCR_002823). Volume-based spatial normalization to two standard spaces (MNI152NLin2009cAsym, MNI152NLin6Asym) was performed through nonlinear registration with antsRegistration (ANTs 2.3.3), using brain-extracted versions of both T1w reference and the T1w template. The following templates were selected for spatial normalization: ICBM 152 Nonlinear Asymmetrical template version 2009c [Fonov et al., 2009, RRID:SCR_008796; TemplateFlow ID: MNI152NLin2009cAsym], FSL's MNI ICBM 152 non-linear 6th Generation Asymmetric Average Brain Stereotaxic Registration Model [Evans et al., 2012 , RRID:SCR_002823; TemplateFlow ID: MNI152NLin6Asym].

Functional data preprocessing

For each of the 1 BOLD runs found per subject (across all tasks and sessions), the following preprocessing was performed. First, a reference volume and its skull-stripped version were generated using a custom methodology of fMRIPrep. Head-motion parameters with respect to the BOLD reference (transformation matrices, and six corresponding rotation and translation parameters) are estimated before any spatiotemporal filtering using mcflirt (Jenkinson et al., 2002; FSL 6.0.5.1:57b01774). The estimated fieldmap was then aligned with rigid-registration to the target EPI (echo-planar imaging) reference run. The field coefficients were mapped on to the reference EPI using the transform. The BOLD reference was then co-registered to the T1w reference using mri_coreg (FreeSurfer) followed by flirt (Jenkinson & Smith, 2001; FSL 6.0.5.1:57b01774) with the boundary-based registration (Greve & Fischl, 2009) cost-function. Co-registration was configured with six degrees of freedom. Several confounding time-series were calculated based on the preprocessed BOLD: framewise displacement (FD), DVARS and three region-wise global signals. FD was computed using two formulations following Power (absolute sum of relative motions, Power et al., 2014) and Jenkinson (relative root mean square displacement between affines, Jenkinson et al., 2002). FD and DVARS are calculated for each functional run, both using their implementations in Nipype (following the definitions by Power et al. 2014).

The three global signals are extracted within the CSF, the WM, and the whole-brain masks. Additionally, a set of physiological regressors were extracted to allow for component-based noise correction (CompCor, Behzadi et al., 2007). Principal components are estimated after high-pass filtering the preprocessed BOLD time-series (using a discrete cosine filter with 128s cut-off) for the two CompCor variants: temporal (tCompCor) and anatomical (aCompCor). tCompCor components are then calculated from the top 2% variable voxels within the brain mask. For aCompCor, three probabilistic masks (CSF, WM and combined CSF+WM) are generated in anatomical space. The implementation differs from that of Behzadi et al. in that instead of eroding the masks by 2 pixels on BOLD space, the aCompCor masks are subtracted a mask of pixels that likely contain a volume fraction of GM. This mask is obtained by thresholding the corresponding partial volume map at 0.05, and it ensures components are not extracted from voxels containing a minimal fraction of GM. Finally, these masks are resampled into BOLD space and binarized by thresholding at 0.99 (as in the original implementation). Components are also calculated separately within the WM and CSF masks. For each CompCor decomposition, the k components with the largest singular values are retained, such that the retained components' time series are sufficient to explain 50 percent of variance across the nuisance mask (CSF, WM, combined, or temporal). The remaining components are dropped from consideration. The head-motion estimates calculated in the correction step were also placed within the corresponding confounds file. The confound time series derived from head motion estimates and global signals were expanded with the inclusion of temporal derivatives and quadratic terms for each (Satterthwaite et al., 2013). Frames that exceeded a threshold of 0.5 mm FD or 1.5 standardised DVARS were annotated as motion outliers. The BOLD time-series were resampled into standard space, generating a preprocessed BOLD run in MNI152NLin2009cAsym space. First, a reference volume and its skull-stripped version were generated using a custom methodology of fMRIPrep. Automatic removal of motion artifacts using independent component analysis (ICA-AROMA, Pruim et al., 2015) was performed on the preprocessed BOLD on MNI space time-series after removal of non-steady state volumes and spatial smoothing with an isotropic, Gaussian kernel of 6mm FWHM (full-width half-maximum). Corresponding "non-aggresively" denoised runs were produced after such smoothing. Additionally, the "aggressive" noise-regressors were collected and placed in the corresponding confounds file. All resamplings can be performed with a single interpolation step by composing all the pertinent transformations (i.e. head-motion transform matrices, susceptibility distortion correction when available, and co-registrations to anatomical and output spaces). Gridded (volumetric) resamplings were performed using antsApplyTransforms (ANTs), configured with Lanczos interpolation to minimize the smoothing effects of other kernels (Lanczos, 1964). Non-gridded (surface) resamplings were performed using mri_vol2surf (FreeSurfer).

Appendix B

Nodes

Node	Label AAL3	Full anatomical description			
1	Frontal_Sup_2_L	Left superior frontal gyrus, dorsolateral	20	Occipital_Sup_L	Left superior occipital gyrus
2	Frontal_Sup_2_R	Right superior frontal gyrus, dorsolateral	21	Occipital_Sup_R	Right superior occipital gyrus
3	Frontal_Mid_2_L	Left middle frontal gyrus	22	Occipital_Mid_L	Left middle occipital gyrus
4	Frontal_Mid_2_R	Right middle frontal gyrus	23	Occipital_Mid_R	Right middle occipital gyrus
5	Frontal_Sup_Medial_L	Left superior frontal gyrus, medial	24	Parietal_Sup_L	Left superior parietal gyrus
6	Frontal_Sup_Medial_R	Right superior frontal gyrus, medial	25	Parietal_Sup_R	Right superior parietal gyrus
7	Frontal_Sup_Med_Orb_L	Left superior frontal gyrus, medial orbital	26	Parietal_Inf_L	Left inferior parietal gyrus, excluding supramarginal and angular gyri
8	Frontal_Sup_Med_Orb_R	Right superior frontal gyrus, medial orbital	27	Angular_L	Left angular gyrus
9	Rectus_R	Right gyrus rectus	28	Angular_R	Right angular gyrus
10	Cingulate_Mid_L	Left middle cingulate & paracingulate gyri	29	Precuneus_L	Left precuneus
11	Cingulate_Mid_R	Right middle cingulate & paracingulate gyri	30	Precuneus_R	Right precuneus
12	Cingulate_Post_L	Left posterior cingulate gyrus	31	Temporal_Sup_R	Right superior temporal gyrus
13	Cingulate_Post_R	Right posterior cingulate gyrus	32	Temporal_Mid_L	Left middle temporal gyrus
14	Calcerine_L	Left calcarine fissure and surrounding cortex	33	Temporal_Mid_R	Right middle temporal gyrus
15	Calcerine_R	Right calcarine fissure and surrounding cortex	34	Cerebellum_4_5_L	Left lobule IV, V of cerebellar hemisphere
16	Cuneus_L	Left cuneus	35	Cerebellum_4_5_R	Right lobule IV, V of cerebellar hemisphere
17	Cuneus_R	Right cuneus	36	Vermis_4_5	Lobule IV, V of vermis
18	Lingual_L	Left lingual gyrus	37	ACC_pre_L	Left anterior cingulate cortex, preguneal
19	Lingual_R	Right lingual gyrus	38	ACC_pre_R	Right anterior cingulate cortex, preguneal

Note. List of nodes that were used for analysis after applying the DMN mask to the Automated Anatomical Labeling 3 (AAL3) atlas as described by Rolls et al. (2020).

Appendix C

Significant node pairs

	Region 1		Region 2	M	SD	p-value						
26	Parietal_Inf_L	24	Parietal_Sup_L	0,83	0,05	3,2E-42	23	Occipital_Mid_R	22	Occipital_Mid_L	0,26	0,16	4,5E-10
33	Temporal_Mid_R	31	Temporal_Sup_R	0,73	0,05	2,9E-40	27	Angular_L	22	Occipital_Mid_L	0,25	0,15	1,3E-09
11	Cingulate_Mid_R	10	Cingulate_Mid_L	0,72	0,07	1,2E-34	19	Lingual_R	18	Lingual_L	0,21	0,14	7,4E-09
3	Frontal_Mid_2_L	1	Frontal_Sup_2_L	0,73	0,08	3,6E-33	27	Angular_L	26	Parietal_Inf_L	0,20	0,15	6,5E-08
4	Frontal_Mid_2_R	2	Frontal_Sup_2_R	0,71	0,08	6,3E-33	28	Angular_R	27	Angular_L	0,28	0,21	7,0E-08
30	Precuneus_R	29	Precuneus_L	0,62	0,08	2,5E-30	21	Occipital_Sup_R	20	Occipital_Sup_L	0,18	0,13	9,0E-08
13	Cingulate_Post_R	12	Cingulate_Post_L	0,65	0,09	1,4E-29	28	Angular_R	25	Parietal_Sup_R	0,21	0,16	1,1E-07
18	Lingual_L	14	Calcerine_L	0,59	0,09	1,2E-28	29	Precuneus_L	10	Cingulate_Mid_L	0,15	0,11	2,5E-07
20	Occipital_Sup_L	16	Cuneus_L	0,53	0,09	7,8E-27	36	Vermis_4_5	13	Cingulate_Post_R	0,14	0,11	2,7E-07
19	Lingual_R	15	Calcerine_R	0,43	0,09	4,1E-24	33	Temporal_Mid_R	23	Occipital_Mid_R	0,15	0,12	2,8E-07
30	Precuneus_R	17	Cuneus_R	0,48	0,10	9,9E-24	29	Precuneus_L	27	Angular_L	0,15	0,13	1,9E-06
15	Calcerine_R	14	Calcerine_L	0,49	0,11	2,6E-22	29	Precuneus_L	24	Parietal_Sup_L	0,14	0,12	2,4E-06
34	Cerebellum_4_5_L	18	Lingual_L	0,50	0,12	6,2E-22	8	Frontal_Sup_Med_Orb_R	6	Frontal_Sup_Medial_R	0,22	0,19	3,0E-06
36	Vermis_4_5	19	Lingual_R	0,53	0,13	7,7E-22	36	Vermis_4_5	35	Cerebellum_4_5_R	0,14	0,13	6,6E-06
28	Angular_R	23	Occipital_Mid_R	0,49	0,12	5,3E-21	25	Parietal_Sup_R	24	Parietal_Sup_L	0,15	0,14	1,5E-05
38	ACC_pre_R	6	Frontal_Sup_Medial_R	0,51	0,13	1,8E-20	29	Precuneus_L	14	Calcerine_L	0,12	0,12	1,7E-05
21	Occipital_Sup_R	17	Cuneus_R	0,38	0,10	1,8E-20	30	Precuneus_R	11	Cingulate_Mid_R	0,14	0,14	2,3E-05
35	Cerebellum_4_5_R	19	Lingual_R	0,51	0,14	2,2E-20	16	Cuneus_L	12	Cingulate_Post_L	0,10	0,11	1,9E-04
8	Frontal_Sup_Med_Orb_R	7	Frontal_Sup_Med_Orb_L	0,59	0,16	8,4E-20	35	Cerebellum_4_5_R	17	Cuneus_R	0,09	0,11	3,9E-04
37	ACC_pre_L	6	Frontal_Sup_Medial_R	0,48	0,13	8,7E-20	37	ACC_pre_L	5	Frontal_Sup_Medial_L	0,13	0,15	4,1E-04
17	Cuneus_R	16	Cuneus_L	0,40	0,11	9,7E-20	22	Occipital_Mid_L	20	Occipital_Sup_L	0,11	0,13	4,1E-04
37	ACC_pre_L	7	Frontal_Sup_Med_Orb_L	0,44	0,13	2,4E-19	24	Parietal_Sup_L	17	Cuneus_R	0,09	0,10	5,1E-04
16	Cuneus_L	14	Calcerine_L	0,34	0,10	9,0E-19	6	Frontal_Sup_Medial_R	5	Frontal_Sup_Medial_L	0,13	0,16	1,1E-03
25	Parietal_Sup_R	21	Occipital_Sup_R	0,39	0,13	9,5E-18	30	Precuneus_R	15	Calcerine_R	0,12	0,15	1,2E-03
9	Rectus_R	8	Frontal_Sup_Med_Orb_R	0,45	0,16	4,0E-16	38	ACC_pre_R	37	ACC_pre_L	0,14	0,18	1,4E-03
30	Precuneus_R	13	Cingulate_Post_R	0,28	0,10	4,6E-16	22	Occipital_Mid_L	13	Cingulate_Post_R	0,07	0,10	2,8E-03
31	Temporal_Sup_R	28	Angular_R	0,33	0,12	6,7E-16	2	Frontal_Sup_2_R	1	Frontal_Sup_2_L	0,12	0,15	2,9E-03
13	Cingulate_Post_R	11	Cingulate_Mid_R	0,27	0,10	1,9E-15	30	Precuneus_R	28	Angular_R	0,11	0,15	3,0E-03
29	Precuneus_L	12	Cingulate_Post_L	0,24	0,10	1,7E-14	24	Parietal_Sup_L	20	Occipital_Sup_L	0,09	0,13	7,3E-03
32	Temporal_Mid_L	22	Occipital_Mid_L	0,33	0,13	1,8E-14	16	Cuneus_L	1	Frontal_Sup_2_L	0,08	0,13	0,014
26	Parietal_Inf_L	22	Occipital_Mid_L	0,34	0,15	5,7E-14	18	Lingual_L	17	Cuneus_R	0,08	0,12	0,015
29	Precuneus_L	16	Cuneus_L	0,25	0,13	3,2E-12	28	Angular_R	2	Frontal_Sup_2_R	0,09	0,14	0,027
17	Cuneus_R	15	Calcerine_R	0,26	0,13	5,4E-12	30	Precuneus_R	19	Lingual_R	0,08	0,13	0,037
23	Occipital_Mid_R	21	Occipital_Sup_R	0,28	0,16	6,7E-11	26	Parietal_Inf_L	12	Cingulate_Post_L	0,06	0,10	0,040
35	Cerebellum_4_5_R	34	Cerebellum_4_5_L	0,23	0,13	6,9E-11	30	Precuneus_R	26	Parietal_Inf_L	0,06	0,11	0,046
32	Temporal_Mid_L	27	Angular_L	0,23	0,13	8,6E-11	36	Vermis_4_5	29	Precuneus_L	0,06	0,11	0,049
12	Cingulate_Post_L	10	Cingulate_Mid_L	0,22	0,13	3,3E-10	32	Temporal_Mid_L	10	Cingulate_Mid_L	0,06	0,10	0,049

Note. All significant ($p < 0,05$) node pairs with a positive mean partial correlation. M = mean, SD = standard deviation.

Appendix D

Matrix of significant node pairs

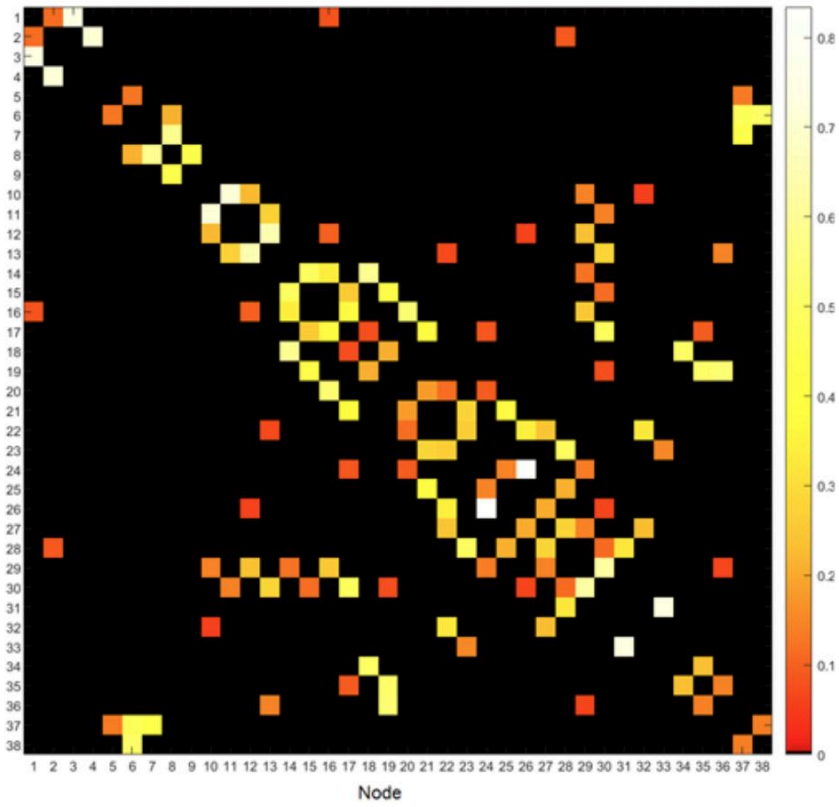

Note. All significant ($p < 0,05$) node pairs with a positive mean partial correlation visualized in a matrix. The mean partial correlation of the significant pairs are represented by a color. The mean negative and unsignificant pairs, as well as the diagonal are set to zero.